atmosphere

MDPI

Article

Quantifying the Attenuation of Leaked CO_2 Through Overlying Strata: Buffer Effects and Surface Signal Detectability

Xinwen Wang [1,2,3], Chaobin Guo [1,3,*], Cai Li [1,3,*] and Qingcheng He [1,3]

1 Chinese Academy of Geological Sciences, Beijing 100037, China
2 School of Water Resources and Environment, China University of Geosciences (Beijing), Beijing 100083, China
3 Technology Innovation Center for Carbon Sequestration and Geological Energy Storage, Ministry of Natural Resources of the People's Republic of China, Beijing 100037, China
* Correspondence: guochaobin@cags.ac.cn (C.G.); licai@cags.ac.cn (C.L.)

Abstract

Defining the near-surface signal reflecting the deep sub-surface leakage is a critical challenge in the risk assessment of geologic carbon storage (GCS) projects, often exacerbated by decoupled deep-to-shallow modeling. This study quantifies the mass distribution and phase evolution of leaked CO_2 through deep reservoir-caprocks, intermediate aquifer, and near-surface soil, thereby showing the sub-surface retention characteristics and the detectability of near-surface signals. A geological model from the deep reservoir to the soil layer was constructed to simulate CO_2 leakage through the caprock and migration into overlying strata in 1000 years. Using the simulator of GPSFLOW, this study evaluates the evolution of fluid phases and the mass distribution during the injection for 100 years and the post-injection periods. The results indicate that (1) at the moment the injection ceases, 87.43–99.06% of the CO_2 remaining within the system is retained within the reservoirs, with less than 8.42% reaching the intermediate aquifer. Remarkably, although the CO_2 ultimately reaching the near-surface soil is less than 0.00073% of the total mass retained within the system, this mass accumulation translates to a concentration anomaly with a signal-to-noise ratio of 368 relative to the background baseline. (2) Sensitivity analysis reveals that the injection rate affects the timing of fluid transport—a tenfold increase in injection rate (from 3.17 to 31.7 kg/s) accelerates the upward movement of CO_2, advancing its arrival at the near-surface by 15 years without changing the overall mass partitioning. The permeability anisotropy ratio affects CO_2 migration and phase distribution—decreasing the vertical to horizontal permeability ratio (1, 0.5, 0.25, 0.125) reduces connectivity, which delays the upward transfer and increases the amount of the aqueous CO_2. However, specifically in the soil layer, the aqueous CO_2 accumulation reveals a non-monotonic trend that peaks at an intermediate ratio of 0.25. (3) CO_2 shows a cascading distribution across formations where reservoirs provide the primary storage, and the intermediate aquifer reduces the mass available for near-surface accumulation. This attenuation effect significantly reduces the CO_2 mass that reaches the soil layer, thereby controlling the strength and duration of near-surface environmental signals. This work offers a theoretical reference for formulating near-surface monitoring strategies for CO_2 leakage in GCS.

Keywords: CO_2 geological storage; leakage; numerical simulation; near-surface detectability

Academic Editors: Liang Huang, Xiaojun Wu, Tao Zhang and Wentong Zhang

Received: 2 March 2026
Revised: 3 April 2026
Accepted: 7 April 2026
Published: 14 April 2026

1. Introduction

Geologic carbon storage (GCS) has been globally recognized as a pivotal mitigation strategy to achieve carbon neutrality and combat climate change [1,2]. The success of

large-scale storage projects, such as those at Sleipner in the North Sea [3] and Weyburn in Canada [4], has demonstrated the technical viability of sequestering CO_2 in deep formations. Ensuring the integrity of the storage complex over the long term necessitates comprehensive monitoring frameworks to detect and quantify potential CO_2 leakage from possible failures [5,6]. Accurately delineating CO_2 plume migration and ensuring sequestration stability has traditionally relied on deep-seated geophysical arrays, such as time-lapse 3D seismic and downhole sensing, as demonstrated at the Sleipner site [7]. While these high-resolution techniques are excellent at verifying reservoir integrity, their sustained implementation in gigatonne-scale GCS operations faces significant challenges regarding operational logistics and economic scalability [2,8,9]. To complement deep reservoir surveys, growing attention has been directed toward sensor applications in the intermediate aquifer and soil layer. Building upon the foundational concepts introduced in previous work [10–13], shallow monitoring is an important approach for reducing project expenses without sacrificing essential environmental protection [14–16].

Despite the significant economic advantages of near-surface monitoring, the interpretation of acquired signals is hindered by the absence of a robust deep-to-shallow coupling mechanism. Upward migrating CO_2 is not a simple direct flux; rather, it undergoes a pronounced cascading interception effect within the stratigraphic column [17–19]. This hierarchical architecture acts as a sequential filter, where secondary trapping mechanisms, primarily dissolution and residual gas trapping, exert powerful mass attenuation and temporal retardation on the rising plume [20,21]. Recent studies have highlighted that intermediate aquifers and low-permeability baffles sequester a substantial portion of the leaked mass, thereby reconfiguring the signal transmission from the deep sub-surface to the shallow environment [22]. Furthermore, transport within the vadose zone introduces additional complexities, as CO_2 undergoes multi-phase distribution and biological interaction, which significantly modifies the geochemical signature before it reaches the atmosphere [23–25]. Without a quantitative understanding of these sub-surface migration dynamics and mass partitioning patterns, near-surface monitoring strategies risk being physically ungrounded, leading to suboptimal sensor placement or the severe misinterpretation of attenuated signals.

Existing studies have made significant advancements in understanding CO_2 plume evolution and local trapping mechanisms within target storage formations. For instance, long-term monitoring and simulations of the Sleipner project have provided in-depth insights into multi-layered plume spreading characteristics under the coupled effects of buoyancy, viscous, and capillary forces [3,21]. Furthermore, relative permeability hysteresis has been demonstrated to be the critical microscopic mechanism governing plume immobilization and residual gas trapping [26,27]. During the cross-formational migration of CO_2 following the breach of the primary caprock, the concept of secondary accumulation has been proposed to explain the buffering and attenuating effects of intermediate formations on leaked fluids [28], and vertical equilibrium models alongside multi-layered semi-analytical solutions have been widely applied for basin-scale pressure and plume assessments [20,29,30]. However, many current studies tend to decouple deep storage reservoirs from near-surface environments, treating them as isolated systems [25,31,32]. When assessing near-surface leakage risks, these studies frequently rely on simplified theoretical calculations or uncoupled boundary fluxes to estimate the CO_2 mass arriving at the near-surface [32,33]. Consequently, the specific retention mass, dynamic gas–liquid phase partitioning, and inter-formational attenuation of CO_2 within intermediate strata along the pathway still require quantification.

In this study, a deep-to-shallow geological model is constructed to simulate the multi-formational migration of CO_2 through a localized weak zone within the caprock. The key

contribution of this work lies in the end-to-end quantitative linkage between deep subsurface leakage dynamics and near-surface monitoring detectability. We quantified the mass distribution among various stratigraphic compartments and performed sensitivity analyses to evaluate the detectability of near-surface signals induced by an assumed leakage. This work offers a theoretical basis for designing near-surface monitoring networks for CO_2 leakage.

2. Methods

This study constructed a comprehensive deep-to-shallow numerical model. Accordingly, this chapter details the geological framework construction, property parameterization, and simulation scenario design.

2.1. Geological Concept Model

A generalized 3D geological model (9000 m × 9000 m × 2250 m) was developed to represent a comprehensive sedimentary sequence, deep reservoir-caprocks, intermediate aquifer, and near-surface. The thicknesses of the reservoir and caprock were simplified and generalized based on nine representative caprock cases, resulting in two sets of reservoirs and caprock (Table 1, Figure 1). The depth of the soil layer was determined with reference to geological conditions in the Shengli Oilfield (Figure 1). China's first million-ton CCUS project, the Qilu Petrochemical and Shengli Oilfield CCUS Project, was constructed here and has been in operation since 2022. Available data and field investigations indicate that the phreatic aquifer is 1–2 m below the ground surface.

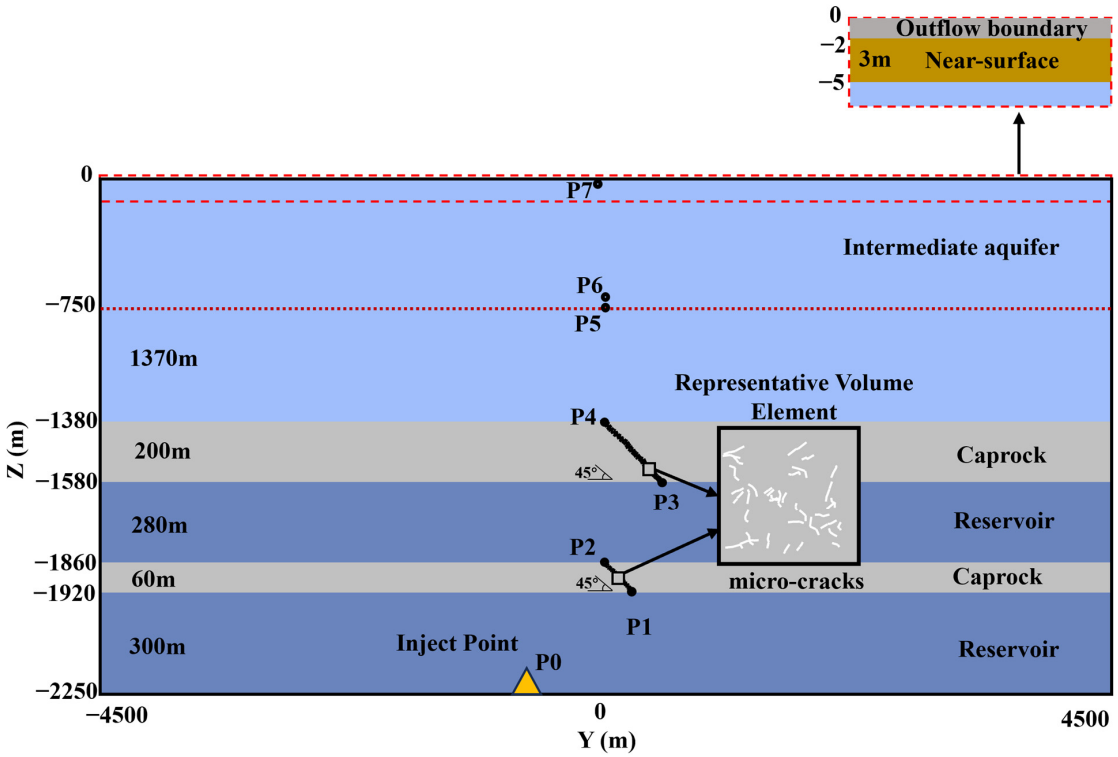

Figure 1. Geological concept model.

A potential leakage risk is attributed to a pre-existing, sub-seismic fracture zone dipping at 45°, representing a typical normal fault geometry that is often critically stressed and optimally oriented for failure under regional stress regimes [34,35]. This fracture is strategically situated 350 m from the injection point. This setup is designed to simulate a hidden leakage pathway, providing sufficient spatial buffering for initial trapping mechanisms to operate while driving complex upward and lateral fluid movement [20,33]. In the GPS-

FLOW simulation framework, this zone is represented using the Equivalent Continuum Model [36,37]. In this approach, the collective hydraulic conductivity of the distributed micro-fractures is homogenized into anisotropic effective permeability tensors assigned to the corresponding discretized grid blocks, thereby creating a preferential flow path that captures the leakage potential of these subtle features. Monitoring points were located directly above the fracture-controlled leakage outlet to capture the maximum localized anomalies resulting from upward CO_2 migration. The geological concept model is shown in Figure 1.

Table 1. Depth and thickness range of million-ton-scale land-based reservoir storage projects.

No.	Project Name	Country	Reservoir Depth (m)	Reservoir Thickness (m)	Primary Caprock Thickness (m)	Secondary Caprock Depth (m)	Secondary Caprock Thickness (m)
1	In Salah [38,39]	Algeria	1800	20	200	/	750
2	South West Hub Project [40]	Australia	1400	1500	700	/	450
3	Boundary Dam [41]	Canada	3200–3400	168	15	/	150
4	Illinois Industrial [42]	USA	2129–2149	500	151	Seal 1: 1500–2000; Seal 2: 1000–1500	20–30, 30–50
5	Kemper [43]	USA	1200–1700	180	180	/	/
6	Fort Nelson [44,45]	Canada	2000	44	50	/	200
7	Quest [46]	Canada	1850–2500	400	550	/	/
8	Weyburn [47]	Canada	1350–1450	30	10–30	600–1000	50–100
9	Michigan [48]	USA	1646	105	/	/	/

2.2. GPSFLOW Simulator

GPSFLOW is a General Purpose Sub-surface Flow Simulator. It solves the governing equations for non-isothermal, multiphase, multicomponent flows in porous or fractured media. The GPSFLOW simulation capabilities are diverse. Its main application covers geological CO_2 sequestration, geothermal reservoir engineering, nuclear waste isolation studies, environmental assessment and remediation, gas/energy sub-surface storage, unconditional oil/gas production, and flow and transport in variably saturated media and aquifers. This simulator can calculate for different phases of CO_2, within the temperature range of 3–300 °C and the pressure range of 0.1–72.5 MPa, including three distinct fluid phases: a liquid phase rich in CO_2 containing dissolved water (liquid phase), an aqueous phase composed primarily of water with dissolved CO_2 (aqueous phase), and a gaseous phase rich in CO_2 that may also hold water (gaseous phase).

The governing equations solved in GPSFLOW are the same as the well-known simulators such as TOUGH, OpenGeoSys and DuMUx [49–51]. The numerical accuracy of the simulator was evaluated through benchmark comparisons with the widely used TOUGH family of simulators, including tests of multiphase flow and CO_2 leakage along fault zones. Good agreement was observed in key variables such as pressure, saturation, and temperature. The solver is formulated based on mass and energy conservation principles with adaptive time stepping, ensuring stable and reliable performance for long-term simulations.

Conservation of mass and energy

$$\frac{d}{dt}\int_{V_n} M^i dV_n = \int_{\Gamma_n} F^i \cdot n d\Gamma_n + \int_{V_n} q^i dV_n \quad (1)$$

V_n: an arbitrary subdomain bounded by the closed surface Γ_n; M^i: mass or energy accumulation term of component i per volume; F: mass or heat flux; n: normal vector on the surface element $d\Gamma_n$ pointing toward V_n; and q: sink/source term of mass or energy.

Mass accumulation

$$M^i = \phi \sum_{\beta}^{NPH} S_\beta \rho_\beta X_\beta^i \quad (2)$$

$$i = 1, NK; \beta = 1, NPH$$

ϕ: porosity; β: phase index (e.g., β = gas, aqueous phase); S_β: saturation of phase β (the volume fractions of the pore space occupied by each phase); ρ_β: density of phase β; X_β^i: mass fraction of component i in phase β; NK: number of components; and NPH: number of phases.

Energy accumulation

$$M^{NK+1} = \Phi \sum_{\beta=1}^{NPH} S_\beta \rho_\beta U_\beta + (1-\Phi)\rho_R C_R T \quad (3)$$

U_β: specific internal energy of phase β; ρ_R: rock density; C_R: rock specific heat; and T: temperature.

Mass flux

$$F^i = \sum_{\beta=1}^{NPH} X_\beta^i \rho_\beta u_\beta \quad (4)$$

u_β: Darcy's velocity (volume flux) of component i in phase β. Diffusive mass flux is ignored as it is smaller compared with the advective mass flux.

Phase velocity

$$u_\beta = -k \frac{k_{r\beta}}{\mu_\beta} (\nabla P_\beta - \rho_\beta g) \quad (5)$$

k: absolute permeability; $k_{r\beta}$: relative permeability to phase β; μ_β: dynamic viscosity of phase β; P_β: pressure in phase β; and g: gravitational acceleration

Energy flux

$$F^{NK+1} = -\lambda \nabla \mathrm{T} + \varphi \sum_{\beta=1}^{NPH} h_\beta \rho_\beta u_\beta \quad (6)$$

λ: thermal conductivity and h_β: specific enthalpy in phase β.

To ensure computational efficiency while maintaining physical rigor, several key simplifying assumptions were integrated into the numerical model. First, the fluid–rock system is treated as isothermal. Second, the governing equations focus on pressure-driven advection and capillary-driven flow, with molecular diffusion being omitted. While molecular diffusion governs mass transfer under static conditions [52], pressure-driven advection dominates CO_2 transport in permeable or fractured pathways, extending into the shallow vadose zone [53,54]. Excluding lateral diffusion from the governing equations confines the simulated CO_2 plume to the primary migration conduit, thereby yielding an upper bound estimate for localized peak concentrations.

2.3. Model Setup

2.3.1. Domain Discretization

In this study, the computational domain is discretized using a non-uniform structured grid. To accurately capture the high-saturation regions of the CO_2 plume resulting from leakage through caprock micro-cracks, a multi-level nested refinement structure is implemented. As shown in Figure 2, this structure radiates outward, with its center specifically targeting the vertical migration path of the plume. The core refinement zone employs a grid size of 40 × 40 m, and the grid size in the transition zone is progressively coarsened to 60 × 60 m and 200 × 200 m, while the far-field boundary zone is further expanded to coarse grids of 600 × 600 m. This graded discretization scheme effectively reduces computational redundancy in non-critical far-field regions while ensuring high resolution in the core leakage area. Vertically, the horizontally refined area extends through the entire model thickness, precisely covering the potential leakage channel migrating upward from the deep aquifer through the caprock micro-cracks. The vertical domain is discretized into a total of 126 grid cells. The numerical domain is discretized into a total of 189,558 grid cells.

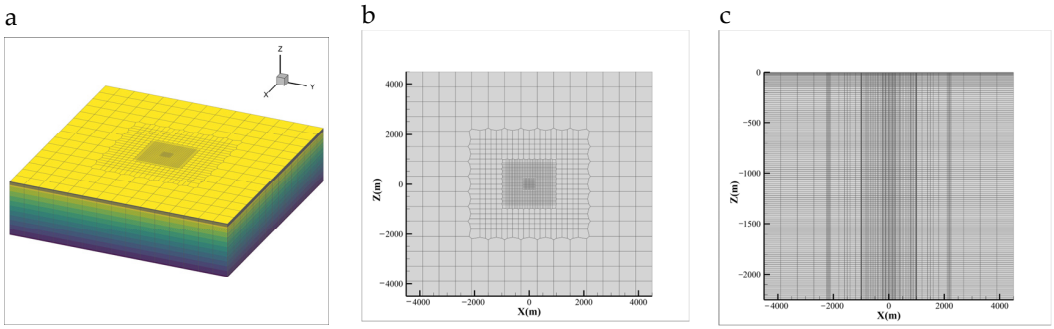

Figure 2. Discretization of the computational domain using a structured grid. (**a**) 3D mesh; (**b**) XZ section mesh; (**c**) XY section mesh.

2.3.2. Rock Properties

Capillary pressure and relative permeability curves were represented using the van Genuchten model [55,56]. The petrophysical and two-phase flow parameters used in this study were derived from existing GCS benchmark models and field tests [57]. For the soil layer and the intermediate aquifer, intrinsic properties and van Genuchten parameters were based on the Zero Emission Research and Technology (ZERT) shallow release model [21]. For the deep reservoir and caprock, petrophysical properties were adopted from the Sleipner project benchmark to represent a sandstone–shale storage complex. Additionally, the two-phase flow characteristics for the deep formations were sourced from previous CO_2 leakage simulations [25,27]. The baseline model parameters are summarized in Table 2.

Table 2. Properties of the layers in the model.

	Near-Surface (Soil)	Intermediate Aquifer (Cobble)	Reservoir Layers (Porous Medium)	Caprock Layers (Porous Medium)
Porosity(Ø)	0.35	0.35	0.27	0.12
Permeability (k)	5×10^{-11} m^2	3.2×10^{-12} m^2	1×10^{-12} m^2	1.0×10^{-18} m^2
Capillary Pressure (Pc)	van Genuchten λ = 0.291, Slr = 0.15 $\alpha = 2.04 \times 10^{-4}$ Pa^{-1} Pmax = 1×10^5 Pa, Sls = 1	van Genuchten λ = 0.627, Slr = 0.10 $\alpha = 1.48 \times 10^{-3}$ Pa^{-1} Pmax = 1×10^5 Pa, Sls = 1	van Genuchten λ = 0.457, Slr = 0.10 $\alpha = 1.48 \times 10^{-3}$ Pa^{-1} Pmax = 1×10^5 Pa, Sls = 1	van Genuchten λ = 0.457, Slr = 0.10 $\alpha = 1.48 \times 10^{-3}$ Pa^{-1} Pmax = 1×10^5 Pa, Sls = 1
Relative permeability (kr)	van Genuchten Slr = 0.35, Sgr = 0.05	van Genuchten Slr = 0.30, Sgr = 0.05	van Genuchten Slr = 0.30, Sgr = 0.05	van Genuchten Slr = 0.30, Sgr = 0.05

2.3.3. Initial and Boundary Conditions

The upper boundary of the model is defined as a constant atmospheric pressure boundary, allowing gas to escape in order to represent the open conditions of the actual ground surface. The lower boundary is specified as a no-flow boundary to prevent both fluid and heat transfer. The lateral boundaries are treated as symmetry boundaries, with a sufficient distance maintained between the lateral boundary and the injection well to minimize boundary effects on the simulation results. The initial condition of the model assumes hydrostatic pressure equilibrium, and the temperature distribution is prescribed based on a geothermal gradient of 0.03 °C/m. The CO_2 concentration in the system is assumed to be zero.

2.4. Case Design

The simulation specifies an active leakage period with a cumulative CO_2 injection of 10^{10} kg, followed by an extended period of well closure. This temporal design is structured to capture the upward fluid migration driven by pressure during the active phase, and the plume evolution, lateral spreading, and phase transitions dominated by buoyancy during the relaxation period. In terms of scenario parameter configuration, the model adjusts the injection rate to represent varying degrees of deep containment failure. Anisotropy parameters are introduced based on the research of Guo and Wang [18] to reflect differences between vertical and horizontal permeability. A *kv*/*kh* gradient ranging from 1 to 0.125 was established to represent varying

degrees of vertical connectivity and the restrictive effect of horizontal stratigraphic baffles [18,21]. Concurrently, the permeability of the localized leakage pathway is assigned using data from Li et al. [58] to reasonably characterize the highly permeable structural features that facilitate the upward migration of CO_2 (Table 3). Case1-1 serves as the base case.

Table 3. Case parameters.

	Injection Rate (kg/s)	Injection Time (Years)	*kv*/*kh* Ratio
case1-1	3.17	100	1
case1-2	3.17	100	0.5
case1-3	3.17	100	0.25
case1-4	3.17	100	0.125
case2-1	6.34	50	1
case2-2	6.34	50	0.5
case2-3	6.34	50	0.25
case2-4	6.34	50	0.125
case3-1	31.7	10	1
case3-2	31.7	10	0.5
case3-3	31.7	10	0.25
case3-4	31.7	10	0.125

3. Results and Discussion

3.1. CO_2 Phase Saturation Distribution in the Base Case

At 100 years, the CO_2 plume develops mainly in the vertical direction with limited horizontal spread (Figure 3a–c). This pattern results from the combination of fracture flow and injection pressure [35,59]. During this stage, because liquid CO_2 is less dense than water, buoyancy drives its continued upward movement [60]. In the meantime, CO_2 dissolved in water (Sa) is mainly found around the edges of the liquid saturation and gas saturation zone (Figure 3b), exhibiting a pattern of accumulation at the margins. This shows that the dissolution of CO_2 into water has started but remains a secondary process, where mass transfer is mainly limited to local dispersion because large-scale convective mixing has not yet developed [61].

At 200 years (Figure 3d–f), the expansion of the plume boundary within the reservoir stabilizes, while internal distribution occurs, particularly within the reservoirs (Figure 3d,e). The core of high gas saturation shrinks, accompanied by a substantial increase in liquid saturation within the same region. This process is caused by the residual trapping mechanism; as injection stops and overpressure drops, buoyancy drives the upward movement of the carbon dioxide tail [32,35]. This leads to the imbibition of surrounding water, which snaps off continuous CO_2 columns into isolated droplets or ganglia by pore-scale capillary forces [60]. Notably, the spatial extent and continuity of gas-phase CO_2 in the intermediate aquifer and soil layers decrease significantly. This shows that the upward gas supply from depth has entered a decay phase after the injection ended.

At 1000 years (Figure 3g–i), gaseous CO_2 is no longer found continuously within the reservoir (Figure 3i), as overall gas saturation remains at low residual levels. Compared to the 200-year stage, regions of high dissolved CO_2 concentration shift from the plume interior toward the edges, forming a clear zone of enrichment at the periphery. This distribution indicates that over long time scales, CO_2 dissolution is marked by mass transfer at the boundaries. The increased density of water saturated with CO_2 triggers gravitational instability, leading to density-driven convection, which accelerates the downward transport of CO_2 into the underlying water [60]. The depletion of the internal gas core limits the dissolution process to the plume edges. In this area, constant contact with fresh water keeps the reaction going [29,61,62].

These results demonstrate that, after the cessation of injection, the spatial distribution of gas and aqueous phases reflects distinct modes of CO_2 occurrence across the reservoir, aquifer, and soil layers. Therefore, a stratified, multi-phase quantification of CO_2 inventories is necessary to characterize the relative retention behavior of different geological units under leakage scenarios.

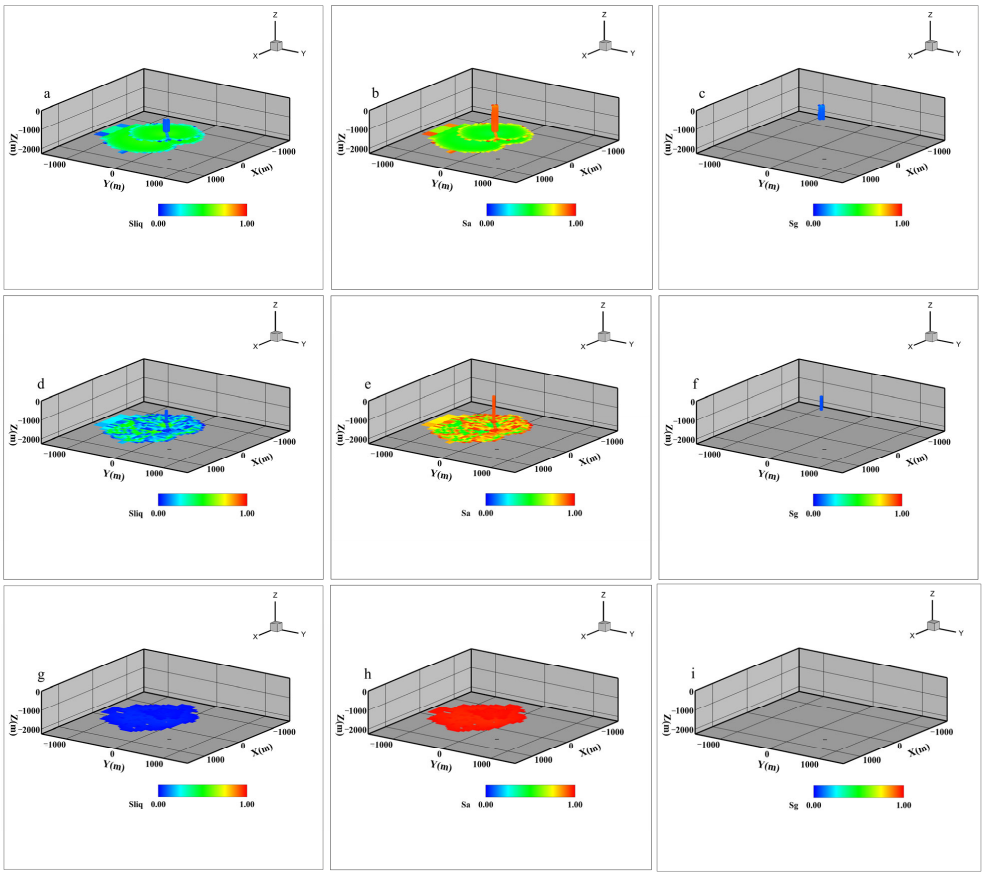

Figure 3. Phase saturation distribution and evolution at (**a**–**c**) 100 years, (**d**–**f**) 200 years, and (**g**–**i**) 1000 years. Sliq: liquid-phase CO_2; Sa: aqueous-phase CO_2; Sg: gaseous-phase CO_2.

3.2. Evolution of CO_2 Phase Saturation in the Base Case

Figures 4–6 illustrate the evolution of phase saturation at monitoring points (as shown in Figure 1) across different stratigraphic units during both the injection and post-injection phases. The clear differences in response strength, duration, and signal shape among these variables show that the distribution and phase evolution of CO_2 are strongly controlled by vertical stratification [3,29]. Vertically, CO_2-related signals exhibit a clear pattern of stepwise attenuation from the deep reservoir toward the near-surface. This attenuation is seen in both the reduced response size and the shorter duration of phase changes and pressure perturbations (Figure 7), consistent with the hierarchical retarding effects of the multi-layered geological system on leaking fluids [31,33].

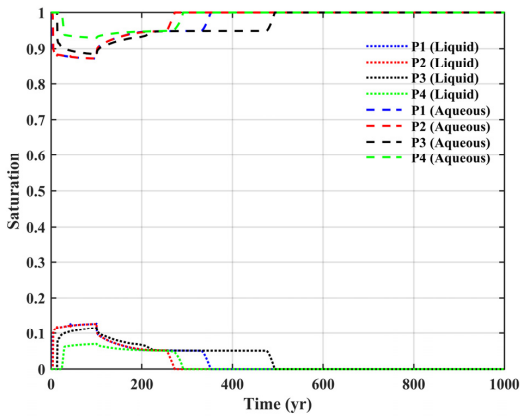

Figure 4. Saturation changes at the crack monitoring points.

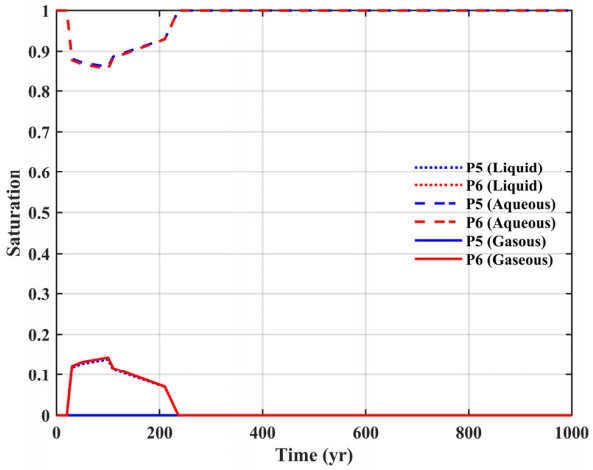

Figure 5. Saturation changes at the intermediate aquifer monitoring points.

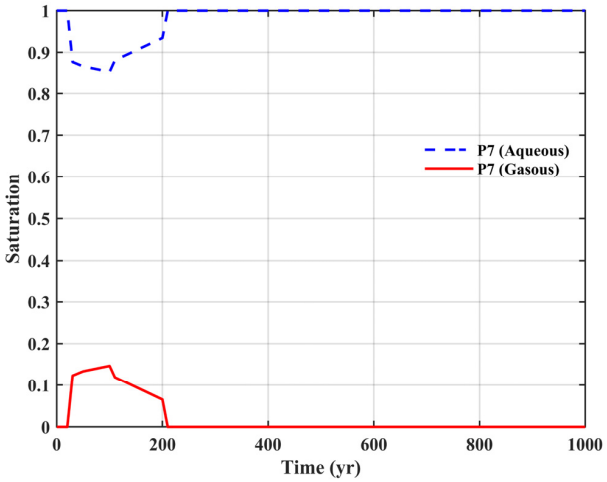

Figure 6. Saturation changes at the monitoring points in the soil.

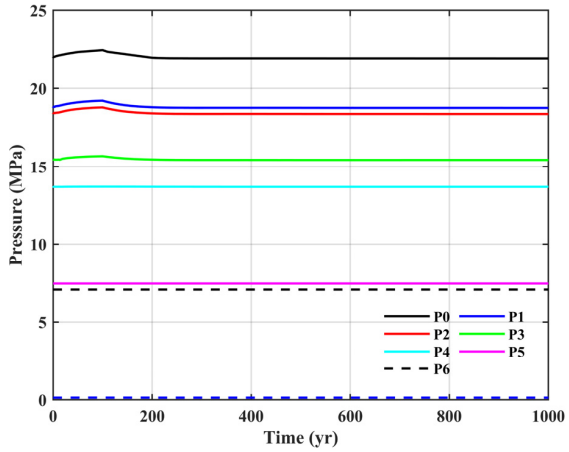

Figure 7. Pressure changes at monitoring points.

At the monitoring points within the injection layer and the fracture, variables exhibit the most direct and significant sensitivity to injection activities, characterized by high strength and long durations. During the evolution process, liquid phase saturation increases markedly, while water saturation declines synchronously due to fluid displacement. Gas saturation remains at zero, showing that under deep high-pressure conditions, CO_2 exists mainly as a liquid, which makes it difficult to form a stable gas phase [35,63]. Therefore,

CO_2 migration is controlled mainly by the distribution between the liquid and aqueous phases. Notably, CO_2 migrating upward along the fracture does not exist exclusively in a liquid state. As the fluid rises and meets lower pressure and temperature conditions in the overburden, the amount of CO_2 dissolved in the aqueous phase changes dynamically. This may be caused by Joule–Thomson cooling or volume expansion [28].

The intermediate aquifer serves as a buffer zone within the hierarchical mass distribution system [28,32]. This unit effectively attenuates the vertical propagation of CO_2 through phase distribution and sub-surface retention mechanisms, such as solubility trapping and capillary trapping [20,64]. Monitoring points show a sequence of rising and falling gas and liquid saturations, followed by a recovery in water saturation as the CO_2 supply from the deep reservoir ends (Figure 6). The lateral spreading and dissolution within this unit reduce the upward mass, thereby increasing the time lag and extending the duration of signals detected near the surface [28,32].

The soil layer represents the terminal stage of hierarchical attenuation, where CO_2 leakage signals are significantly suppressed by preceding stratigraphic units. Monitoring data indicate that liquid, gas, and water saturations, as well as pressure, remain at minimal levels, exhibiting only transient or intermittent fluctuations within a narrow time (Figure 6). Restricted by the transport capacity of deep formations and secondary trapping mechanisms, the upward mass supply is insufficient to sustain a prolonged presence of gaseous CO_2 within the shallow vadose zone [25,57]. Furthermore, CO_2 in the soil tends to migrate laterally above the water table, which spreads the total mass over a much wider area. This lateral movement, combined with the natural gases from soil respiration, makes the leakage signal very faint compared to environmental noise. Therefore, the signal becomes difficult to identify because it is lost within the natural background levels [14].

3.3. CO_2 Mass Distribution in the Base Case

Figure 8 illustrates the hierarchical mass evolution of the system, showing a clear disparity among the deep multi-layered storage formations, intermediate aquifer, and near-surface soil. The primary reservoir (RESE1) retains the vast majority of the injected mass, whereas the accumulated mass in the soil layer (SSOIL) is several orders of magnitude lower. This disparity results directly from the buffering capacity of the caprocks and the intermediate aquifer, which successively attenuate deep leakage and cause the upward mass to decrease [18,32,33]. However, this seemingly negligible CO_2 accumulation in the soil holds critical monitoring significance.

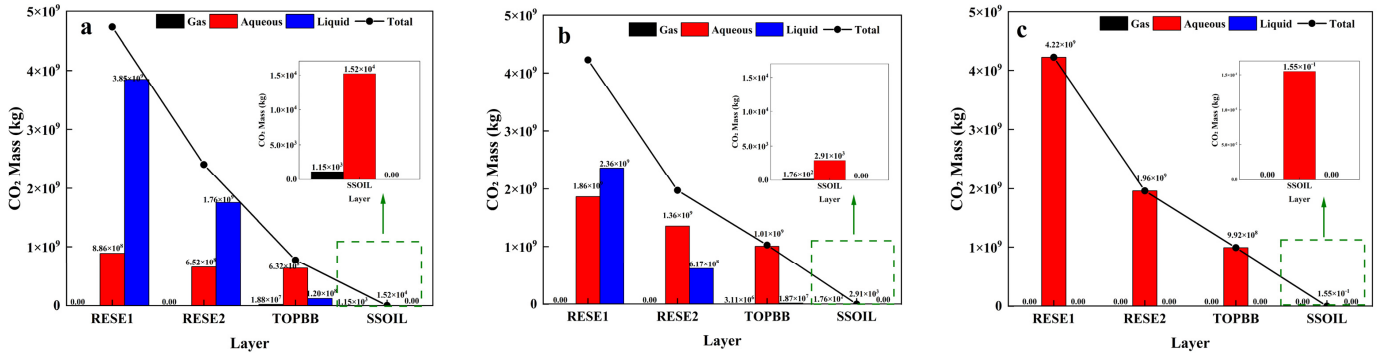

Figure 8. Formation distribution of CO_2 mass at (**a**) 100 years, (**b**) 200 years, and (**c**) 1000 years. (RESE1: primary reservoir; RESE2: secondary reservoir; TOPBB: intermediate aquifer; SSOIL: soil).

The simulation results indicate that CO_2 leaked into the soil primarily evolves into gas and dissolved phases. Although the instantaneous mass burden reaching the shallow sub-surface is low relative to the total inventory, gas-phase CO_2 tends to accumulate in the

soil porous media and form localized high concentration anomalies in the low-pressure vadose zone environment, driven by decompression expansion and diffusion [25]. Previous studies demonstrated that even at low leakage rates (e.g., 0.0002 kg/s), the CO_2 mass fraction at the surface leakage center can reach significant levels (e.g., 0.38–0.48) [25]. As demonstrated by the ZERT and Cranfield projects, modern portable or buried non-dispersive infrared (NDIR) sensors possess sufficient dynamic range and resolution to capture these ppm-level changes in real-time [65]. In case 1-1, the actual retained mass in the soil layer is 15,200 kg at 100 years. At monitoring point P7, the simulated CO_2 mass fraction in the gas phase reached 0.9, which is consistent with the high-concentration core zones observed in the Norwegian field experiments [66]. Even when adopting a conservative spatial average of 736,434 ppm for the monitoring zone, the resulting signal-to-noise (S/N) ratio remains above 368 compared to the typical maximum diurnal soil respiration variability (~2000 ppm). Although the geological overburden greatly attenuates the leakage mass, it does not completely mask these gas-phase signals [9,67,68]. The small amount of leaked mass in the simulation acts as a signal that can be detected. Therefore, near-surface monitoring is effective even without a large seal failure or a blowout, as it can identify small gas-phase changes that reach the surface. By catching these early signals, operators can get an early warning that the sub-surface seal is damaged [25]. The stability of the spatiotemporal distribution characteristics of this precursor signal is constrained by deep dynamic conditions and the attributes of shallow geological media. Existing studies indicate that injection rate and permeability anisotropy can reshape plume morphology by controlling preferential fluid migration pathways [18,21,54]. Therefore, to verify the robustness of near-surface CO_2 signals under varying geological and engineering scenarios, it is necessary to conduct further sensitivity analysis.

3.4. Parametric Analysis

Given that the permeable upper boundary allows for mass transfer, the total mass of CO_2 within the system is not strictly conserved across different scenarios. In this analysis, the mass fraction of each phase is defined as the ratio of the CO_2 mass in a specific phase within a given formation to the total retained mass currently remaining in the system. This metric reflects the relative contribution of various trapping mechanisms to the inventory retained within the sub-surface, excluding any mass leaked to the atmosphere or across boundaries.

3.4.1. Impact of Injection Rate on CO_2 Distribution

Reservoirs

In the primary reservoir, the accumulation of liquid-phase CO_2 during the initial injection period is determined by the dynamic competition between strong external displacement and internal dissolution conversion. During the active injection phase, the mass fraction of the liquid phase rises, indicating that the input rate of liquid CO_2 exceeds its conversion rate into the aqueous phase via dissolution mechanisms. As injection ceases and the liquid supply is cut off, solubility trapping gradually becomes dominant, leading to a significant rebound in the aqueous phase fraction.

Sensitivity analysis reveals that, while maintaining a constant total injection mass, alteration in injection rate (3.17, 6.34, and 31.7 kg/s) significantly changes the time of phase evolution (Figure 9a–c). Higher injection rates result in a much faster accumulation of the liquid phase within the primary reservoir, with peaks reached at 3, 2, and 1 years, respectively. Consequently, the time when the dissolved phase begins to exceed the liquid phase comes earlier as the injection rate increases (occurring at 228, 224, and 183 years, respectively). Notably, by 1000 years, the final aqueous mass fraction under the high

injection (31.7 kg/s) rate scenario (57.14%) is elevated compared to the lower rate (3.17 kg/s) scenario (51.01%). This phenomenon is attributed to the fact that higher injection rates enhance viscous forces, thereby improving sweep efficiency [26]. The resulting expansion in pore volume contact increases the gas–water interfacial area, which in turn intensifies long-term mass transfer efficiency and solubility trapping capacity [60].

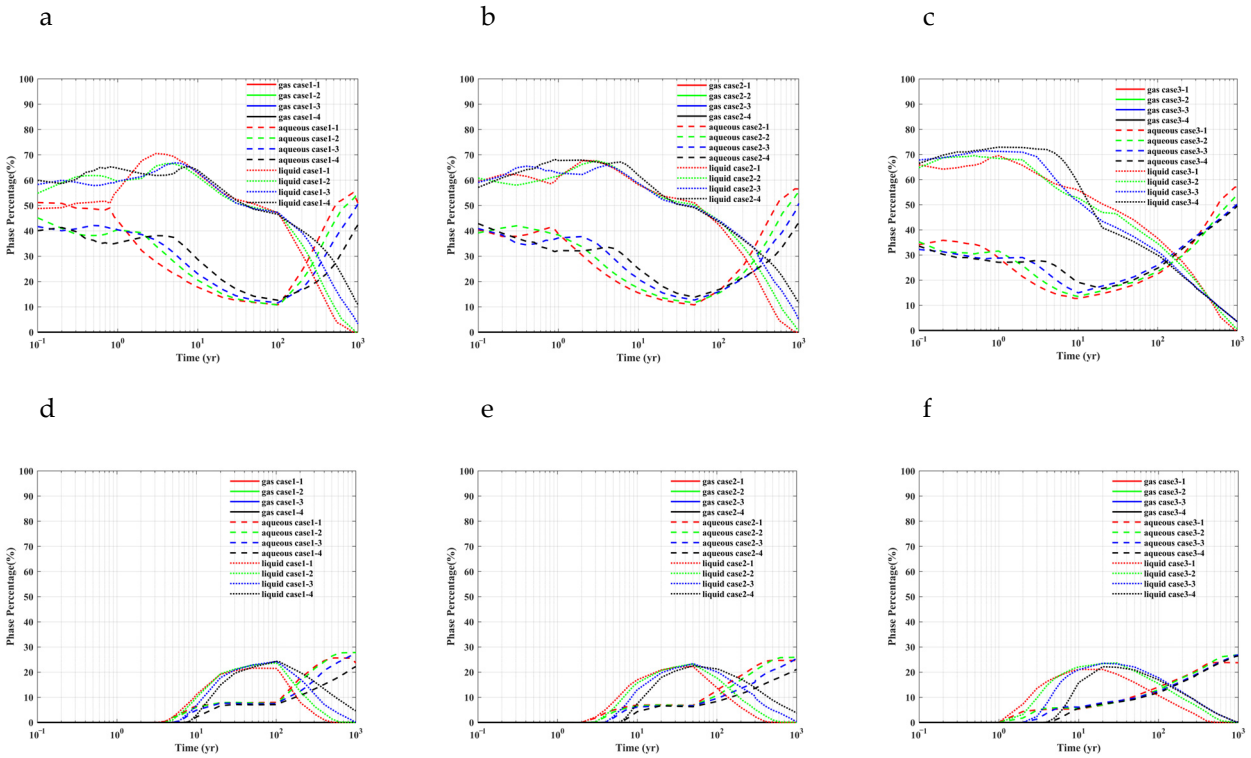

Figure 9. Evolution of CO_2 mass ratios among different phases within the (**a**–**c**) primary reservoir and (**d**–**f**) secondary reservoir.

When CO_2 enters the secondary reservoir through leakage pathways, the time of liquid saturation peaks (at 100, 50, and 10 years) aligns closely with the termination of injection (Figure 9d–f). This suggests that the rapid increase in the liquid fraction within this layer is mainly driven by the advective flux sustained during the injection period [30]. The termination of injection marks a critical inflection point, where the mechanism of phase evolution transitions swiftly from input control to transformation control, dominated by buoyancy segregation and dissolution. Despite substantial variations in injection rates, the peak liquid mass fractions (21.09–22.27%) and the final aqueous mass fractions at 1000 years (23.67–24.60%) within the secondary reservoir exhibit negligible differences. This indicates that, under the condition of constant total mass, an increase in the instantaneous injection rate does not result in a proportional accumulation of liquid phase within the secondary reservoir. The high mass CO_2 input is likely redistributed through two pathways. First, accelerated dissolution into formation water is facilitated by rapid plume expansion. Second, continued upward migration of excess CO_2 along preferential pathways to shallower horizons, driven by local overpressure, rather than retention within the secondary reservoir [34]. Consequently, the primary impact of the injection rate on the secondary reservoir lies in temporal regulation, specifically advancing the arrival of peak saturation.

Intermediate Aquifer

The simulation results indicate that under high injection rates, the arrival time of CO_2 in the intermediate aquifer (Cobble layer) is significantly advanced, exhibiting complex multi-

phase flow characteristics where liquid, gas, and aqueous phases coexist. Sensitivity analysis reveals that across an injection rate gradient of 3.17, 6.34, and 31.7 kg/s (corresponding to injection durations of 100, 50, and 10 years, respectively), the peak liquid mass fractions are 1.54%, 1.64%, and 1.47% (Figure 10a–c). Although high injection rates accelerate fluid migration through the medium by enhancing the driving force, thereby significantly advancing the timing of peak saturation, they do not lead to a marked increase in peak magnitude. This phenomenon reveals that the intermediate aquifer functions primarily as a mechanism of temporal regulation for the leakage plume, rather than acting as a container for mass amplification [28]. This is because at high flow velocities, although the rate of CO_2 entry into the intermediate aquifer increases, the fluid does not accumulate there for extended periods. Instead, it continues to migrate to shallower layers driven by buoyancy or becomes attenuated via lateral dispersion. Similarly, the appearance of gas-phase peaks shows clear time dependence, occurring at 100, 50, and 20 years, with peak values of 0.23%, 0.27%, and 0.25%, respectively (Figure 10a–c). The emergence and rapid dissipation of the gas phase suggest that in the intermediate aquifer, the free gas phase is an unstable transient form, with its existence constrained by pressure maintenance and sustained flux supply during injection. In all the simulated scenarios, an identical long-term evolutionary trend is observed following the cessation of injection, as pressure dissipates, liquid and gas saturations continuously decay to zero, while the aqueous phase fraction expands or reaches a stable plateau. By year 1000, the aqueous mass fractions for the three cases are 11.97%, 11.79%, and 11.79%, respectively (Figure 10 a, b, c). Despite the substantial disparity in injection intensity (a tenfold difference in rates), the proportion ultimately converted to the dissolved state remains highly consistent. This confirms the high stability of solubility trapping as a long-term mechanism.

In summary, while high-pressure injection drives the accelerated vertical migration of CO_2 toward shallow zones and alters the timescale of plume arrival, it does not fundamentally change the sequestration capacity characteristics of the intermediate aquifer. Functioning as an effective secondary trap, the intermediate aquifer converts leaked free fluids into a stable aqueous state via dissolution, thereby consistently mitigating environmental risks across different injection rates.

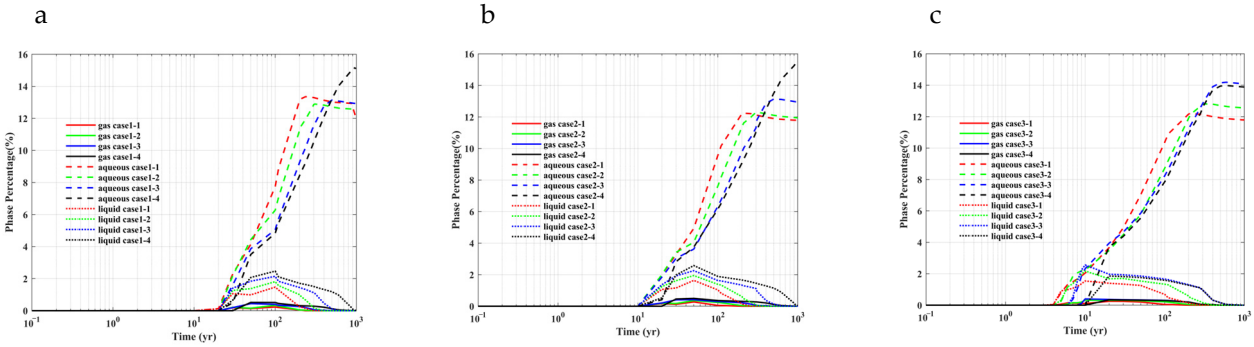

Figure 10. Evolution of CO_2 mass ratios among different phases within the intermediate aquifer. (**a**) The injection rate is 3.17 kg/s; (**b**) The injection rate is 6.34 kg/s; (**c**) The injection rate is 31.7 kg/s.

Soil Layer

In the soil layer, the injection rate primarily shifts the arrival time of shallow signals while exerting minimal influence on the decay timescales dominated by near-surface dissipation and boundary leakage after injection cessation. This results in a pronounced temporal advancement of signal emergence alongside a highly synchronized disappearance. Specifically, the breakthrough time of shallow CO_2 displays a strong dependence on the deep injection rate. The simulation results indicate that as the injection rate increases from 3.17 kg/s to 31.7 kg/s, the arrival time for both aqueous and gas-phase CO_2 advances

markedly from 20 years to 5 years (Figure 11a,c). This inverse relationship confirms that during the active leakage phase, pressure-driven advection plays a dominant role. However, once the deep supply terminates, CO_2 mass across all the scenarios decays synchronously to zero by approximately 210 years, indicating that the shallow attenuation phase exhibits significantly reduced sensitivity to the initial injection rate. In the absence of diffusive transport in this simulation, signal dissipation is driven by a combination of physical mechanisms, the rapid dissipation of advective drive prevents the gas from overcoming capillary resistance for upward migration [52,60], gravity slumping causes the dense residual gas to settle or spread laterally above the water table rather than venting [25,54], and dissolution trapping continuously depletes the gas inventory via phase transfer into mobile soil water [25,60]. Therefore, the time needed for dissipation depends on reservoir properties, such as permeability, the contact area between gas and water, and dissolution rates, rather than the initial injection rate. This explains why the curves from different injection scenarios eventually meet over extended periods.

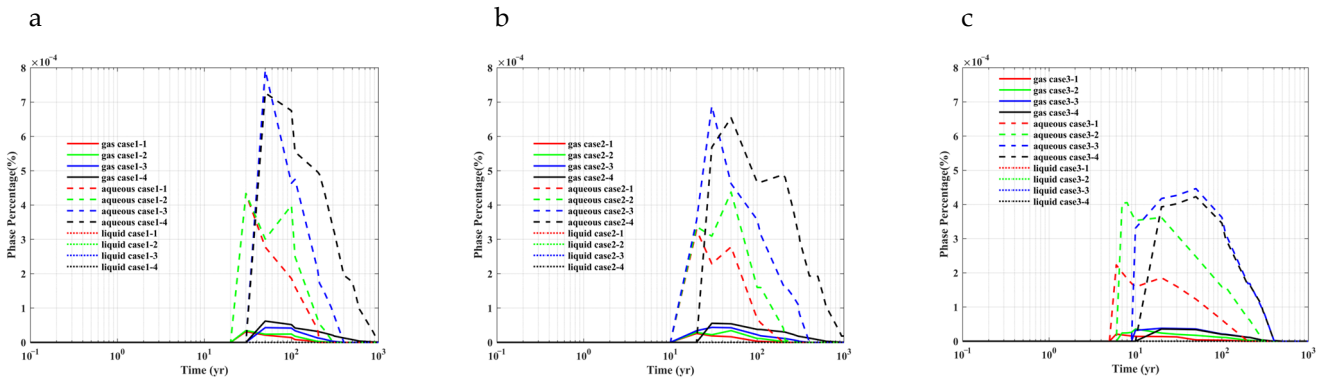

Figure 11. Evolution of CO_2 mass ratios among different phases within the soil. (**a**) The injection rate is 3.17 kg/s; (**b**) The injection rate is 6.34 kg/s; (**c**) The injection rate is 31.7 kg/s.

3.4.2. Impact of Permeability Anisotropy on CO_2 Distribution Reservoirs

Under constant injection rates, as the *kv*/*kh* ratio decreases from 1 to 0.5, 0.25, and 0.125, the liquid phase proportion within the primary reservoir exhibits a broader peak plateau and a more protracted decay phase (Figure 9a–c). Correspondingly, the increase in the aqueous phase mass fraction becomes more gradual, and the temporal intersection between the liquid phase and the aqueous phase is significantly postponed. This retention of the liquid phase is attributed to increased vertical flow resistance, which reduces vertical permeability and suppresses buoyancy-driven upward migration, forcing the fluid into more extensive lateral spreading [18,69]. This modification of the flow regime restricts contact between the liquid phase and unsaturated fresh water, thereby significantly retarding the progress of solubility trapping. As noted by Ennis-King et al. [70] and Riaz et al. [71], a reduction in vertical permeability increases the critical onset time for density-driven convection and suppresses its development. Consequently, the conversion efficiency from the liquid to the aqueous phase diminishes, causing the intersection point of the two phases to be postponed substantially. This effect of impeded vertical transport extends to the secondary reservoir (Figure 9d–f), manifesting as a significant lag in the breakthrough times of both liquid and aqueous phases. This observation aligns with the findings of Birkholzer and Zhou [72] regarding delayed pressure dissipation in multi-layered systems. In summary, while permeability anisotropy does not alter the ultimate thermodynamic equilibrium of dissolution [68,73], by simultaneously constraining vertical seepage and convective mixing, it significantly prolongs the duration of free-phase CO_2 and expands its lateral footprint.

Intermediate Aquifer

The intermediate aquifer serves as a critical buffer zone, where retention and phase transformation determine the leakage mass reaching the shallow sub-surface. Figure 10 illustrates the phase evolution of CO_2 under varying injection rates and permeability anisotropy ratios (*kv*/*kh* from 1 to 0.125). A consistent trend across all the scenarios is the steady increase in the final aqueous phase mass fraction as the *kv*/*kh* ratio decreases. This increased dissolution happens because the lower vertical permeability creates a barrier effect that restricts rapid upward movement [18]. Consequently, the CO_2 plume is forced to transition from vertically dominated flow to extensive lateral spreading, which increases the gas–water interfacial area [69]. This increased sweep volume intensifies mass transfer, effectively transforming the intermediate aquifer from a simple leakage conduit into an efficient dissolution reactor. Regarding the free mobile phases (liquid and gas), strong anisotropy results in both peak amplification and prolonged dissipation. As indicated by the saturation curves in Figure 10, a reduction in *kv*/*kh* leads to higher peak concentrations compared to isotropic conditions. This occurs because the restricted vertical pathways force CO_2 to accumulate locally within the aquifer pores rather than escaping rapidly to the overburden [18]. Furthermore, this impedance induces a time lag effect, significantly extending the residence time of the mobile plume within the formation. This prolonged containment provides a wider temporal window for solubility and capillary trapping mechanisms to operate [26,69].

Soil Layer

In the soil layer, while low *kv*/*kh* increases the gas phase inventory via dissipation limits, it reduces dissolution efficiency by inhibiting convective mass transfer mechanisms. In the vadose zone, CO_2 behaves as a dense gas, and its atmospheric release is primarily governed by vertical seepage [23,54,57]. The low vertical permeability functions as a barrier, impeding prompt escape and compelling the plume to undergo extensive lateral spreading, which results in transient accumulation within shallow pore spaces [18]. Comparatively, the aqueous phase peak occurs at an intermediate anisotropy level (*kv*/*kh* = 0.25), exhibiting a non-monotonic trend (Figure 11). This indicates that effective solubility trapping requires an optimal balance between residence time and mass transfer efficiency. Although lower vertical permeability helps prolong the contact time of CO_2, severe vertical flow resistance suppresses density-driven convection when the *kv*/*kh* ratio further decreases to 0.125 [70,71].

3.5. Mass Distribution and Implications for Near-Surface Monitoring

Figure 12 illustrates the mass partitioning across various simulation scenarios, specifically extracted at two critical time points: the exact moment of injection cessation under different injection rates, and the 200-year simulation mark. At the conclusion of injection (with consistent total injected mass), the inter-formational mass partitioning of CO_2 across the reservoir, intermediate aquifer, and soil compartments remains generally consistent across all the simulation cases (Figure 12). Approximately 87.43–99.06% of the CO_2 is retained within the primary and secondary reservoir units, while 0–8.42% is distributed within the intermediate aquifer, with the mass fraction in the soil layer ranging from 0% to 0.00073%. Although phase proportions within each formation vary under different *kv*/*kh* conditions, these discrepancies do not manifest in the inter-formational mass distribution at the critical juncture of injection cessation. This suggests that CO_2 migration and phase evolution during the injection stage are primarily governed by continuous mass input supply. Under high injection pressure, the influence of vertical permeability anisotropy on inter-formational partitioning remains relatively constrained. By 200 years, the proportion of the aqueous phase within the intermediate aquifer generally increases, while the gas phase and liquid phase fractions decline significantly. Meanwhile, mass proportions in the soil layer remain at minimal levels with no trend of

sustained amplification, indicating that CO_2 entering the soil layer does not accumulate over the long term. Crucially, as discussed in Section 3.3, this tiny amount of CO_2 is still a very important monitoring signal. This confirms that the soil layer acts as a sensitive indicator for finding leakage pathways, even when most of the mass is safely trapped deep underground.

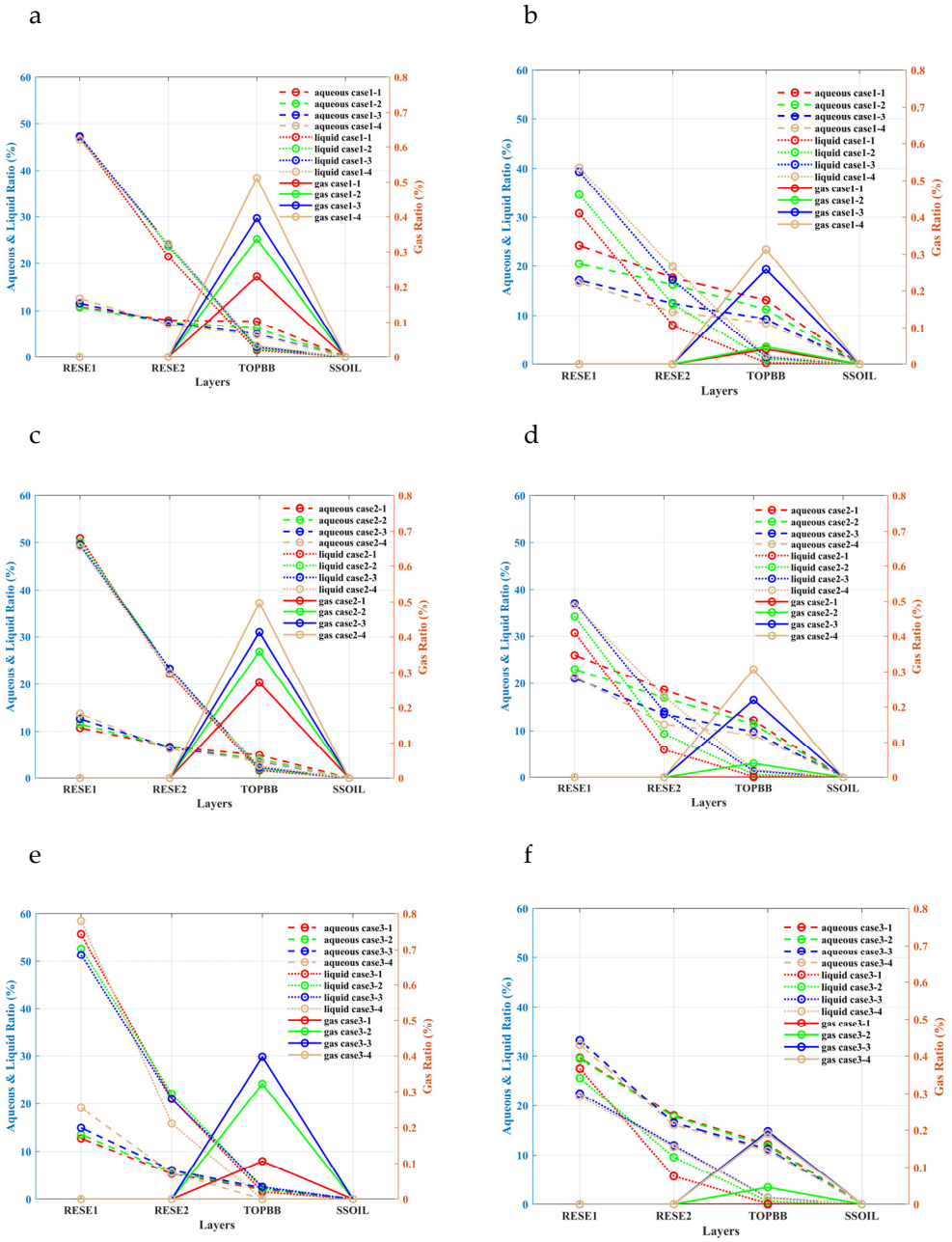

Figure 12. Formation distribution of CO_2 mass ratio in case1 ((**a**): 100 years, (**b**): 200 years); case2 ((**c**): 50 years, (**d**): 200 years); and case3 ((**e**): 10 years, (**f**): 200 years). (RESE1: primary reservoir; RESE2: secondary reservoir; TOPBB: intermediate aquifer; SSOIL: soil).

4. Conclusions

This study provides a quantitative assessment for interpreting environmental risks by effectively linking deep geological leakage with the detectability of signals at the surface. Through characterization of mass distribution and phase evolution within a stratified geological system spanning from the deep reservoir to the soil in the near-surface, the research evaluates the regulatory roles of the injection rate and permeability anisotropy

on fluid retention in the sub-surface. The results of this study support the following key conclusions:

(1) Based on the numerical scenarios examined, at injection cessation, 87.43–99.06% of the leaked CO_2 is retained within the primary and secondary reservoirs, with less than 8.42% reaching the intermediate aquifer. Remarkably, although the CO_2 ultimately reaching the shallow soil layer accounts for less than 0.00073% of the total mass retained within the system, this mass accumulation translates to a concentration anomaly with a signal-to-noise ratio of 368 relative to the background baseline. This estimated signal indicates that leakages are theoretically detectable under idealized transport pathways.

(2) Within the scope of this numerical study, sensitivity analysis reveals that the injection rate affects the timing of fluid transport. Specifically, a tenfold increase in injection rate (from 3.17 kg/s to 31.7 kg/s) accelerates the upward movement of CO_2, advancing its arrival at the near-surface by 15 years without changing the overall mass partitioning. The permeability anisotropy ratio affects CO_2 migration and phase distribution. Decreasing the vertical to horizontal permeability ratio (1, 0.5, 0.25, 0.125) reduces connectivity, which delays the upward transfer and increases the amount of the aqueous CO_2. However, specifically in the soil layer, the aqueous CO_2 accumulation reveals a non-monotonic trend that peaks at an intermediate ratio of 0.25 due to the critical balance between prolonged residence time and density-driven convection.

(3) CO_2 exhibits a cascading, mass-limited distribution across formations, with the reservoirs providing primary storage and the intermediate aquifer progressively reducing the mass available for shallow accumulation. This multi-layered attenuation mechanism significantly reduces the CO_2 mass reaching the soil layer, thereby governing the magnitude and persistence of near-surface environmental signals.

This study provides a robust evaluation of the long-term leakage and evolution characteristics of CO_2. However, as with any large-scale numerical simulation, the current model incorporates certain simplifying assumptions. First, regarding the physical mechanisms, the governing equations do not include the molecular diffusion process. While advection heavily dominates in fracture leakage scenarios driven by strong pressure gradients, neglecting diffusion helps establish a worst-case scenario without lateral dissipation, thus providing an upper-bound estimate for localized peak concentrations. This assumption does not fully capture the lateral spatial spreading of the CO_2 plume caused by matrix diffusion in realistic geological settings. Second, regarding the geological model construction, the deep geological features were moderately simplified in this study. This may not fully reflect the potential impacts of complex three-dimensional heterogeneity at actual sites, such as the fine-scale architecture of multi-layered formations, on multiphase flow migration pathways.

To address these limitations, future work will integrate site-specific data from actual storage sites. Future numerical models will incorporate more refined 3D geological architectures to accurately characterize the structures of deep fault zones and the heterogeneity of multi-layered formations. Furthermore, systematic sensitivity analyses on the spatial locations and geometric configurations (e.g., dip angles and connectivity) of potential leakage pathways will be conducted to cover a wider range of failure scenarios. Additionally, future research will translate these theoretical insights into practical standards for near-surface leakage detection. These findings can directly guide the design of surface monitoring networks, including the optimization of sensor spacing and measurement bounds. Ultimately, this will provide reliable theoretical and technical support for environmental risk assessments and early warning systems in carbon storage projects.

Author Contributions: X.W.: conceptualization, writing—original draft preparation, and software and formal analysis; C.G.: methodology, writing—review and editing, software and formal analysis, and funding acquisition; C.L.: methodology, writing—review and editing, and funding acquisition; Q.H.: investigation, validation, and resources. All authors have read and agreed to the published version of the manuscript.

Funding: National Natural Science Foundation of China (U2344226, U2244215, 42372286); Chinese Geological Survey Projects (DD20221819).

Institutional Review Board Statement: Not applicable.

Informed Consent Statement: Not applicable.

Data Availability Statement: The data presented in this study are available upon request from the corresponding author.

Acknowledgments: We appreciate the anonymous reviewers for their invaluable comments and suggestions on this manuscript.

Conflicts of Interest: The authors declare no conflicts of interest.

Abbreviations

CCUS	Carbon Capture, Utilization and Storage
CO_2	Carbon Dioxide
GCS	Geological Carbon Sequestration
GPSFLOW	General Purpose Sub-surface Flow Simulator
RESE1	Primary Reservoir
RESE2	Secondary Reservoir
SSOIL	Soil Layer
TOPBB	Intermediate Aquifer
Sa	Aqueous-phase CO_2
Sg	Gaseous-phase CO_2
Sliq	Liquid-phase CO_2

References

1. Metz, B.; Davidson, O.; De Coninck, H.; Loos, M.; Meyer, L. *IPCC Special Report on Carbon Dioxide Capture and Storage*; Cambridge University Press: Cambridge, UK, 2005.
2. Global CCS Institute. *Global Status of CCS 2025*; Global CCS Institute: Melbourne, Australia, 2025.
3. Furre, A.-K.; Eiken, O.; Alnes, H.; Vevatne, J.N.; Kiær, A.F. 20 years of monitoring CO_2-injection at Sleipner. *Energy Procedia* **2017**, *114*, 3916–3926. [CrossRef]
4. Beaubien, S.E.; Jones, D.; Gal, F.; Barkwith, A.; Braibant, G.; Baubron, J.-C.; Ciotoli, G.; Graziani, S.; Lister, T.; Lombardi, S. Monitoring of near-surface gas geochemistry at the Weyburn, Canada, CO_2-EOR site, 2001–2011. *Int. J. Greenh. Gas Control.* **2013**, *16*, S236–S262. [CrossRef]
5. Sori, A.; Moghaddas, J.; Abedpour, H. Comprehensive review of experimental studies, numerical modeling, leakage risk assessment, monitoring, and control in geological storage of carbon dioxide: Implications for effective CO_2 deployment strategies. *Greenh. Gases Sci. Technol.* **2024**, *14*, 887–913. [CrossRef]
6. Li, Q.; Liu, G. Risk assessment of the geological storage of CO_2: A review. *Geol. Carbon Sequestration Underst. Reserv. Behav.* **2016**, 249–284. [CrossRef]
7. Arts, R.; Eiken, O.; Chadwick, A.; Zweigel, P.; Van der Meer, L.; Zinszner, B. Monitoring of CO_2 injected at Sleipner using time-lapse seismic data. *Energy* **2004**, *29*, 1383–1392. [CrossRef]
8. China Petroleum and Chemical Industry Federation; Administrative Center for China's Agenda 21. *China Carbon Capture, Utilization and Storage Progress Report 2025*; China Petroleum and Chemical Industry Federation: Beijing, China, 2025.
9. Zhu, Y.; He, Z.; Wang, H.; Liu, Y. CO_2 leakage in geologic carbon storage: A review of its impacts and detection. *Chem. Eng. J.* **2025**, 168423. [CrossRef]
10. Fahrner, S.; Schäfer, D.; Dahmke, A. A monitoring strategy to detect CO_2 intrusion in deeper freshwater aquifers. *Int. J. Greenh. Gas Control* **2012**, *9*, 262–271. [CrossRef]

11. Kim, H.-J.; Han, S.H.; Kim, S.; Yun, S.-T.; Jun, S.-C.; Oh, Y.-Y.; Son, Y. Characterizing the spatial distribution of CO_2 leakage from the shallow CO_2 release experiment in South Korea. *Int. J. Greenh. Gas Control* **2018**, *72*, 152–162. [CrossRef]
12. Peter, A.; Hornbruch, G.; Dahmke, A. CO_2 leakage test in a shallow aquifer for investigating the geochemical impact of CO_2 on groundwater and for developing monitoring methods and concepts. *Energy Procedia* **2011**, *4*, 4148–4153. [CrossRef]
13. Auken, E.; Doetsch, J.; Fiandaca, G.; Christiansen, A.V.; Gazoty, A.; Cahill, A.G.; Jakobsen, R. Imaging subsurface migration of dissolved CO_2 in a shallow aquifer using 3-D time-lapse electrical resistivity tomography. *J. Appl. Geophys.* **2014**, *101*, 31–41. [CrossRef]
14. Tang, P.; Cao, B. A Review on Ecosystem Monitoring for CO_2 Geological Storage. *ACS Omega* **2025**, *10*, 46309–46322. [CrossRef] [PubMed]
15. Caesary, D.; Song, S.Y.; Yu, H.; Kim, B.; Nam, M.J. A review on CO_2 leakage detection in shallow subsurface using geophysical surveys. *Int. J. Greenh. Gas Control* **2020**, *102*, 103165. [CrossRef]
16. Gal, F.; Pokryszka, Z.; Labat, N.; Michel, K.; Lafortune, S.; Marblé, A. Soil-gas concentrations and flux monitoring at the lacq-rousse CO_2-Geological storage pilot site (French Pyrenean Foreland): From pre-injection to post-injection. *Appl. Sci.* **2019**, *9*, 645. [CrossRef]
17. Manceau, J.-C.; Rohmer, J.; Réveillère, A. Natural mitigation of CO_2 leakage accumulations. *Energy Procedia* **2013**, *37*, 4400–4408. [CrossRef]
18. Guo, C.; Wang, X. Effect of permeability anisotropy on the CO_2 saturation distribution and phase change during a leakage event in a saline aquifer. *Front. Energy Res.* **2024**, *12*, 1372655. [CrossRef]
19. Zheng, L.; Nico, P.; Spycher, N.; Domen, J.; Credoz, A. Potential impacts of CO_2 leakage on groundwater quality of overlying aquifer at geological carbon sequestration sites: A review and a proposed assessment procedure. *Greenh. Gases Sci. Technol.* **2021**, *11*, 1134–1166. [CrossRef]
20. Celia, M.A.; Bachu, S.; Nordbotten, J.M.; Bandilla, K.W. Status of CO_2 storage in deep saline aquifers with emphasis on modeling approaches and practical simulations. *Water Resour. Res.* **2015**, *51*, 6846–6892. [CrossRef]
21. Zhu, C.; Zhang, G.; Lu, P.; Meng, L.; Ji, X. Benchmark modeling of the Sleipner CO_2 plume: Calibration to seismic data for the uppermost layer and model sensitivity analysis. *Int. J. Greenh. Gas Control* **2015**, *43*, 233–246. [CrossRef]
22. Rezk, M.G.; Ibrahim, A.F. Numerical investigation of CO_2 plume migration and trapping mechanisms in the sleipner field: Does the aquifer heterogeneity matter? *Fuel* **2025**, *394*, 135054. [CrossRef]
23. Oldenburg, C.M.; Lewicki, J.L.; Dobeck, L.; Spangler, L. Modeling gas transport in the shallow subsurface during the ZERT CO_2 release test. *Transp. Porous Media* **2010**, *82*, 77–92. [CrossRef]
24. Liu, J.; Yang, F.; Chong, S.; Wen, Q.; Lin, Q. Modeling CO_2 migration in a site-specific shallow subsurface under complex hydrodynamics. *Int. J. Greenh. Gas Control* **2021**, *112*, 103483. [CrossRef]
25. Liu, J.; Yang, F.; Chong, S.; Wen, Q. Numerical simulation of CO_2 leakage in a shallow subsurface layer from a CO_2 geological storage site. *Hydrogeol. J.* **2020**, *28*, 2439–2455. [CrossRef]
26. Juanes, R.; Spiteri, E.; Blunt, M.; Orr, F., Jr. Impact of Relative Permeability Hysteresis on Geologic Storage of CO_2. *Water Resour. Res.* **2006**, *42*, W2148. [CrossRef]
27. Doughty, C. Modeling geologic storage of carbon dioxide: Comparison of non-hysteretic and hysteretic characteristic curves. *Energy Convers. Manag.* **2007**, *48*, 1768–1781. [CrossRef]
28. Pruess, K. Leakage of CO_2 from geologic storage: Role of secondary accumulation at shallow depth. *Int. J. Greenh. Gas Control* **2008**, *2*, 37–46. [CrossRef]
29. Ahmadinia, M.; Shariatipour, S.M.; Andersen, O.; Sadri, M. Benchmarking of vertically integrated models for the study of the impact of caprock morphology on CO_2 migration. *Int. J. Greenh. Gas Control* **2019**, *90*, 102802. [CrossRef]
30. Zhou, Q.; Birkholzer, J.T.; Tsang, C.-F.; Rutqvist, J. A method for quick assessment of CO_2 storage capacity in closed and semi-closed saline formations. *Int. J. Greenh. Gas Control* **2008**, *2*, 626–639. [CrossRef]
31. Alcalde, J.; Flude, S.; Wilkinson, M.; Johnson, G.; Edlmann, K.; Bond, C.E.; Scott, V.; Gilfillan, S.M.; Ogaya, X.; Haszeldine, R.S. Estimating geological CO_2 storage security to deliver on climate mitigation. *Nat. Commun.* **2018**, *9*, 2201. [CrossRef]
32. Kivi, I.R.; Makhnenko, R.Y.; Oldenburg, C.; Rutqvist, J.; Vilarrasa, V. Multi-layered systems for permanent geologic storage of CO_2 at the gigatonne scale. *Geophys. Res. Lett.* **2022**, *49*, e2022GL100443. [CrossRef]
33. Cihan, A.; Birkholzer, J.T.; Zhou, Q. Pressure buildup and brine migration during CO_2 storage in multilayered aquifers. *Groundwater* **2013**, *51*, 252–267. [CrossRef] [PubMed]
34. Rinaldi, A.P.; Rutqvist, J.; Cappa, F. Geomechanical effects on CO_2 leakage through fault zones during large-scale underground injection. *Int. J. Greenh. Gas Control* **2014**, *20*, 117–131. [CrossRef]
35. Shipton, Z.K.; Evans, J.P.; Kirschner, D.; Kolesar, P.T.; Williams, A.P.; Heath, J. Analysis of CO_2 leakage through 'low-permeability' faults from natural reservoirs in the Colorado Plateau, east-central Utah. *Geol. Soc. Lond. Spec. Publ.* **2004**, *233*, 43–58. [CrossRef]
36. Khoei, A.; Ehsani, R.; Hosseini, N. An extended-FEM model for CO_2 leakage through a naturally fractured cap-rock during carbon dioxide sequestration. *Transp. Porous Media* **2022**, *145*, 175–195. [CrossRef]

37. Oda, M. An equivalent continuum model for coupled stress and fluid flow analysis in jointed rock masses. *Water Resour. Res.* **1986**, *22*, 1845–1856. [CrossRef]
38. Mathieson, A.; Midgley, J.; Dodds, K.; Wright, I.; Ringrose, P.; Saoul, N. CO_2 sequestration monitoring and verification technologies applied at Krechba, Algeria. *Lead. Edge* **2010**, *29*, 216–222. [CrossRef]
39. Mathieson, A.; Midgely, J.; Wright, I.; Saoula, N.; Ringrose, P. In Salah CO_2 Storage JIP: CO_2 sequestration monitoring and verification technologies applied at Krechba, Algeria. *Energy Procedia* **2011**, *4*, 3596–3603. [CrossRef]
40. Green, C.; Michael, K.; Paterson, L. Simulation of CO_2 migration for the planning of well test configurations at the South West Hub Project, Western Australia. *Energy Procedia* **2017**, *114*, 3445–3455. [CrossRef]
41. Verdon, J.P.; Kendall, J.-M.; Horleston, A.C.; Stork, A.L. Subsurface fluid injection and induced seismicity in southeast Saskatchewan. *Int. J. Greenh. Gas Control* **2016**, *54*, 429–440. [CrossRef]
42. Strandli, C.W.; Mehnert, E.; Benson, S.M. CO_2 plume tracking and history matching using multilevel pressure monitoring at the Illinois Basin–Decatur Project. *Energy Procedia* **2014**, *63*, 4473–4484. [CrossRef]
43. Wethington, C.; Pashin, J.; Wethington, J.; Esposito, R.; Riestenberg, D. Mudstone baffles and barriers in lower cretaceous strata at a proposed CO_2 storage hub in Kemper County, Mississippi, United States. *Front. Energy Res.* **2022**, *10*, 904850. [CrossRef]
44. Gorecki, C.D.; Liu, G.; Bailey, T.P.; Sorensen, J.A.; Klapperich, R.J.; Braunberger, J.R.; Steadman, E.; Harju, J.A. The role of static and dynamic modeling in the Fort Nelson CCS Project. *Energy Procedia* **2013**, *37*, 3733–3741. [CrossRef]
45. Crockford, P.W. CO_2 storage in a Devonian carbonate system, Fort Nelson British Columbia. *Energy Procedia* **2011**, *4*, 5118–5125.
46. Tawiah, P.; Duer, J.; Bryant, S.L.; Larter, S.; O'Brien, S.; Dong, M. CO_2 injectivity behaviour under non-isothermal conditions–Field observations and assessments from the Quest CCS operation. *Int. J. Greenh. Gas Control* **2020**, *92*, 102843. [CrossRef]
47. Jensen, G.K. Weyburn oilfield core assessment investigating cores from pre and post CO_2 injection: Determining the impact of CO_2 on the reservoir. *Int. J. Greenh. Gas Control* **2016**, *54*, 490–498. [CrossRef]
48. Haagsma, A.; Weber, S.; Moody, M.; Sminchak, J.; Gerst, J.; Gupta, N. Comparative wellbore integrity evaluation across a complex of oil and gas fields within the Michigan Basin and implications for CO_2 storage. *Greenh. Gases Sci. Technol.* **2017**, *7*, 828–842. [CrossRef]
49. Jung, Y.; Pau, G.S.H.; Finsterle, S.; Doughty, C.A. *TOUGH3 User's Guide, Version 1.0*; Lawrence Berkeley National Laboratory: Berkeley, CA, USA, 2018.
50. Flemisch, B.; Darcis, M.; Erbertseder, K.; Faigle, B.; Lauser, A.; Mosthaf, K.; Müthing, S.; Nuske, P.; Tatomir, A.; Wolff, M.; et al. DuMux: DUNE for multi-{phase, component, scale, physics, ...} flow and transport in porous media. *Adv. Water Resour.* **2011**, *34*, 1102–1112. [CrossRef]
51. Kolditz, O.; Bauer, S.; Bilke, L.; Böttcher, N.; Delfs, J.O.; Fischer, T.; Görke, U.J.; Kalbacher, T.; Kosakowski, G.; McDermott, C.I.; et al. OpenGeoSys: An open-source initiative for numerical simulation of thermo-hydro-mechanical/chemical (THM/C) processes in porous media. *Environ. Earth Sci.* **2012**, *67*, 589–599. [CrossRef]
52. Mortezaei, K.; Amirlatifi, A.; Ghazanfari, E.; Vahedifard, F. Potential CO_2 leakage from geological storage sites: Advances and challenges. *Environ. Geotech.* **2021**, *8*, 3–27. [CrossRef]
53. Aminu, M.D.; Nabavi, S.A.; Rochelle, C.A.; Manovic, V. A review of developments in carbon dioxide storage. *Appl. Energy* **2017**, *208*, 1389–1419. [CrossRef]
54. Oldenburg, C.M.; Unger, A.J. On leakage and seepage from geologic carbon sequestration sites: Unsaturated zone attenuation. *Vadose Zone J.* **2003**, *2*, 287–296. [CrossRef]
55. Pruess, K.; Oldenburg, C.; Moridis, G. *TOUGH2 User's Guide Version 2*; Lawrence Berkeley National Laboratory, University of California: Berkeley, CA, USA, 1999; p. 192.
56. Van Genuchten, M.T. A closed-form equation for predicting the hydraulic conductivity of unsaturated soils. *Soil Sci. Soc. Am. J.* **1980**, *44*, 892–898. [CrossRef]
57. Lewicki, J.; Oldenburg, C.; Dobeck, L.; Spangler, L. Surface CO_2 leakage during two shallow subsurface CO_2 releases. *Geophys. Res. Lett.* **2007**, *34*, L24402. [CrossRef]
58. Liu, Y.; Wang, L.; Zhang, L. Prediction on leakage and rate characteristics of CO_2 storage. *CIESC J.* **2012**, *63*, 1226–1233.
59. Siriwardane, H.J.; Gondle, R.K.; Bromhal, G.S. Coupled flow and deformation modeling of carbon dioxide migration in the presence of a caprock fracture during injection. *Energy Fuels* **2013**, *27*, 4232–4243. [CrossRef]
60. Ajayi, T.; Gomes, J.S.; Bera, A. A review of CO_2 storage in geological formations emphasizing modeling, monitoring and capacity estimation approaches. *Pet. Sci.* **2019**, *16*, 1028–1063. [CrossRef]
61. Ghorbani, Z.; Riaz, A.; Daniel, D. Convective mixing in vertically-layered porous media: The linear regime and the onset of convection. *Phys. Fluids* **2017**, *29*, 014102. [CrossRef]
62. Li, Q.; Cai, W.H.; Li, B.X.; Chen, C.-Y. Numerical study of density-driven convection in laminated heterogeneous porous media. *J. Mech.* **2020**, *36*, 665–673. [CrossRef]
63. Nordbotten, J.M.; Celia, M.A.; Bachu, S. Injection and storage of CO_2 in deep saline aquifers: Analytical solution for CO_2 plume evolution during injection. *Transp. Porous Media* **2005**, *58*, 339–360. [CrossRef]

64. Shukla, R.; Ranjith, P.; Haque, A.; Choi, X. A review of studies on CO_2 sequestration and caprock integrity. *Fuel* **2010**, *89*, 2651–2664. [CrossRef]
65. Yang, C.; Romanak, K.D.; Reedy, R.C.; Hovorka, S.D.; Trevino, R.H. Soil gas dynamics monitoring at a CO_2-EOR site for leakage detection. *Geomech. Geophys. Geo-Energy Geo-Resour.* **2017**, *3*, 351–364. [CrossRef]
66. Jones, D.; Barkwith, A.; Hannis, S.; Lister, T.; Gal, F.; Graziani, S.; Beaubien, S.E.; Widory, D. Monitoring of near surface gas seepage from a shallow injection experiment at the CO_2 Field Lab, Norway. *Int. J. Greenh. Gas Control* **2014**, *28*, 300–317. [CrossRef]
67. Risk, D.; Lavoie, M.; Nickerson, N. Using the Kerr investigations at Weyburn to screen geochemical tracers for near-surface detection and attribution of leakage at CCS/EOR sites. *Int. J. Greenh. Gas Control* **2015**, *35*, 13–17. [CrossRef]
68. Jiang, X.; Hassan, W.A.A.; Gluyas, J. Modelling and monitoring of geological carbon storage: A perspective on cross-validation. *Appl. Energy* **2013**, *112*, 784–792. [CrossRef]
69. Gershenzon, N.I.; Soltanian, M.; Ritzi, R.W., Jr.; Dominic, D.F. Influence of small scale heterogeneity on CO_2 trapping processes in deep saline aquifers. *Energy Procedia* **2014**, *59*, 166–173. [CrossRef]
70. Ennis-King, J.; Preston, I.; Paterson, L. Onset of convection in anisotropic porous media subject to a rapid change in boundary conditions. *Phys. Fluids* **2005**, *17*, 084107. [CrossRef]
71. Riaz, A.; Hesse, M.; Tchelepi, H.; Orr, F. Onset of convection in a gravitationally unstable diffusive boundary layer in porous media. *J. Fluid Mech.* **2006**, *548*, 87–111. [CrossRef]
72. Birkholzer, J.T.; Zhou, Q. Basin-scale hydrogeologic impacts of CO_2 storage: Capacity and regulatory implications. *Int. J. Greenh. Gas Control* **2009**, *3*, 745–756. [CrossRef]
73. Jiang, X. A review of physical modelling and numerical simulation of long-term geological storage of CO_2. *Appl. Energy* **2011**, *88*, 3557–3566. [CrossRef]